Surface 3D nanostructuring by tightly focused laser pulse: simulations by Lagrangian code and molecular dynamics

2016 J. Phys.: Conf. Ser. 681 012001

(http://iopscience.iop.org/1742-6596/681/1/012001)

Surface 3D nanostructuring by tightly focused laser pulse: simulations by Lagrangian code and molecular dynamics

Nail A. Inogamov[1] **and Vasily V. Zhakhovsky**[2]

E-mail: `nailinogamov@gmail.com`
[1]Landau Institute for Theoretical Physics, RAS, Chernogolovka, Russia
[2]Dukhov Research Institute of Automatics (VNIIA), Moscow, Russia

Abstract.

There are many important applications in which the ultrashort diffraction-limited and therefore tightly focused laser pulses irradiates metal films mounted on dielectric substrate. Here we present the detailed picture of laser peeling and 3D structure formation of the thin (relative to a depth of a heat affected zone in the bulk targets) gold films on glass substrate. The underlying physics of such diffraction-limited laser peeling was not well understood previously.

Our approach is based on a physical model which takes into consideration the new calculations of the two-temperature (2T) equation of state (2T EoS) and the two-temperature transport coefficients together with the coupling parameter between electron and ion subsystems. The usage of the 2T EoS and the kinetic coefficients is required because absorption of an ultrashort pulse with duration of 10–1000 fs excites electron subsystem of metal and transfers substance into the 2T state with hot electrons (typical electron temperatures 1-3 eV) and much colder ions. It is shown that formation of submicrometer-sized 3D structures is a result of the electron-ion energy transfer, melting, and delamination of film from substrate under combined action of electron and ion pressures, capillary deceleration of the delaminated liquid metal or semiconductor, and ultrafast freezing of molten material. We found that the freezing is going in non-equilibrium regime with strongly overcooled liquid phase. In this case the Stefan approximation is non-applicable because the solidification front speed is limited by the diffusion rate of atoms in the molten material. To solve the problem we have developed the 2T Lagrangian code including all this reach physics in. We also used the high-performance combined Monte-Carlo and molecular dynamics code for simulation of surface 3D nanostructuring at later times after completion of electron-ion relaxation.

1. Introduction

Figure 1 presents typical 2D and 3D structures produced in experiments [1–6] with the thin gold films. Let us call "nanobumps" all such structures. The film "f" and the underlying substrate "s" in Fig. 1 (a) are in solid state before a single laser impact. The final (i.e. long time after impact) nanobumps also are solid. Formation of a nipple in the tip of nanobump in Fig. 1 (c), or the jet in Fig. 1 (d-g) means that gold inside the heated spot have passed the melting stage and have been solidified after melting. The sequence of nanobumps in Fig. 1 (b-g) is shown in ascending order as the central fluence F_c of spatial distribution $F(r) = F_c \exp(-r^2/R_L^2)$ increases; here r is a distance from the axis of laser beam (we suppose the normal incidence) and the spatial scale R_L characterizes a focused laser beam "L" shown in Fig. 1 (a). Pulse duration should be

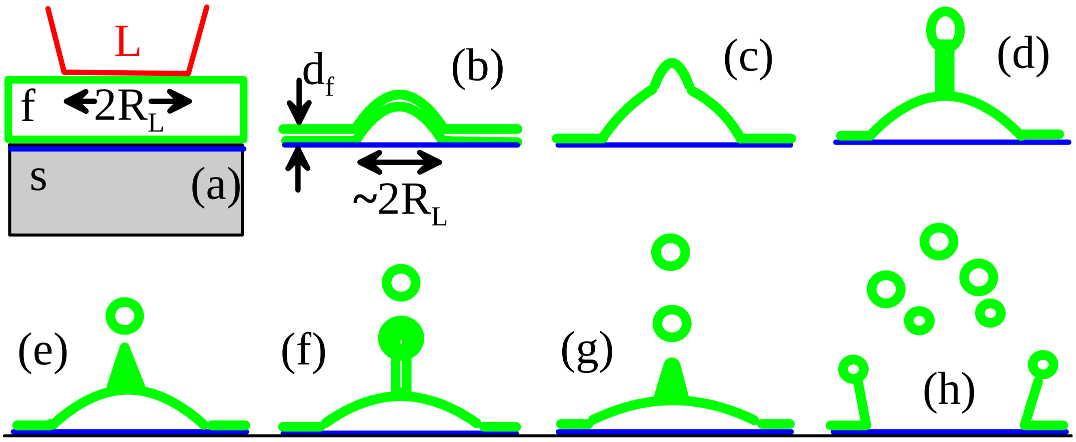

Figure 1. The sequence (b-g) of the nanobumps shown in ascending order as energy of a laser pulse increases while a radius R_L of a laser beam is fixed. Increase of energy at a fixed radius R_L means that the central fluence F_c of a distribution $F = F_c \exp(-r^2/R_L^2)$ increases. A pulse acts onto a layered target composed from a film "f" mounted above a substrate "s". Further increase of F_c above the case (g) results in formation of a hole in a tip region of a nanobump. A radius of the hole (h) increases while length of a delaminated remnants decreases as the F_c increases. In 2D we do not see formation of the long jets. Instead a droplet like condensation in the tip appears. In the 2D/3D cases there are the planar/circular laser beams "L" (a) and the nanobumps are slit type or rounded respectively.

of the order of, or shorter, than an acoustic time scale $t_s = d_f/c_s$ to lead to a *thermomechanical* delamination of film from substrate produced by a stress field generated by fast heating; here d_f is a thickness of film (see Figs. 1 a, b), c_s is sound speed in gold.

Experiments [7] with a femtosecond pulse and a thin $d_f \sim 40$ nm gold film, $t_s \sim 10$ ps demonstrate that the pulse duration τ_L doesn't influence results up to durations at least ≈ 8 ps, see Fig. 2 in [7]. Let us mention that for the thin films the acoustic scale t_s is comparable with the duration of two-temperature electron-ion relaxation t_{eq}; $t_{eq} \approx 5-7$ ps for gold. In a sense of delamination dynamics of separation of a film from a substrate the comparison τ_L versus t_{eq} is insignificant relative to the comparison τ_L versus t_s. In the both mentioned cases the condition $\tau_L < t_s$ ("supersonic" laser pulse) assures that the strong thermomechanical stresses drive the delamination irrespective to the origin of the stress – is it mainly electronic in the subcase $\tau_L < t_s < t_{eq}$, or is it electronic at the two-temperature stage and ionic later in the subcase $\tau_L < t_{eq} < t_s$. There is some quantitative difference [8] between these two subcases because the electronic Gruneisen parameter ≈ 1 is smaller than the ionic Gruneisen parameter ≈ 2. But the situation changes qualitatively in the case of the "subsonic" pulses $\tau_L > t_s$ when amplitude of the mechanical stress drops down as the ratio τ_L/t_s increases above 1.

A fluence distribution $F(r)$ along a surface with a pronounced central $r = 0$ maximum F_c produces a velocity distribution $v(r)$ with a maximum. This is a normal (relative to surface) component v of velocity of a local piece of a film *after* separation of this piece from a substrate (this piece is at a distance r). In experiments a film is thin in the sense that its thickness d_f is much less $d_f \ll R_L$ than the spot size R_L, see Fig. 1 (a); the typical values are: $d_f \sim 20-100$ nm, the radius is $R_L \sim 1$ micron for the cases with diffraction limited focusing and optical lasers. The lateral velocities are small relative to the normal one as a result of this shallowness. The maximum velocity v locates in the center $r = 0$, thus the dome like shapes of the nanobumps shown in Fig. 1 are formed. Duration of an acoustic stage t_s is enough long to homogenize distribution of locally absorbed laser energy across a thickness d_f of a film[1]; but this duration is very short for the temperature equalizing at the distances $\sim R_L \gg d_f$ along a hot spot in Fig. 1. Thus a distribution of energy $E(r)$ per unit of volume appears at the beginning of an acoustic stage. The pressure distribution $p(r)$ acting to delaminate a film [10] is $p(r) \propto E(r)$; because variation of Gruneisen parameter and volume expansion at the beginning of the acoustic stage both are small. If we neglect the adhesion between gold and silica glass then the velocity distribution along a film is $v(r) \propto p(r) \propto E(r) \propto F(r)$.

Firstly, there is a small value of the gold/silica adhesion and, secondly, absorbed energy decays strongly $\propto \exp(-r^2/R_L^2)$ outside the spot $\sim R_L$. Therefore in the external area $r > r_{delam} \sim R_L$ the film remains in mechanical contact with the film as shown in Fig. 1. We will see below that the mechanical contact connecting the internal $r < r_{delam}$ and the external $r > r_{delam}$ parts is important for deceleration of the delaminated film while the thermal contact between the hot dome and the outside cold film is necessary for cooling and freezing of the dome. Increase of the scale r_{delam} with increase of pulse energy $E_{total} \propto F_c$ (if R_L is fixed) has been studied in paper [11], see their plots in the $\ln E, r^2_{delam}$ plane in their Fig. 4. As a result of adhesion between gold and glass the velocity distribution $v(r)$ is equal to zero for the distances $r > r_{delam}$. Thus the velocity distribution $v(r)$ follows the fluence distribution $v(r) \propto F(r)$ everywhere except the margins $r \approx r_{delam}$. Experimentally an interesting situation with a ring type fluence distribution $F(r)$ has been considered [12], see Fig. 8 in this paper. Then complicated motion from the ring to the center is observed.

The droplets shown in Fig. 1 lose the thermal contact and therefore for a long time remain in a liquid state. Estimates of the radiation loses $t_{rad} \sim cTV/(\sigma_{SB} T^4 S) \sim 0.6\,(R_{droplt}/100\text{nm})/(T/2000\text{K})^2$ millisec give large values for the radiative cooling time t_{rad}; here $c \approx 3nk_B$ is heat capacity, $n \approx 6 \cdot 10^{22}$ cm^{-3} is concentration of atoms, k_B is the Boltzmann constant, T is temperature of a droplet after separation from a jet, V, S, R_{droplt} are volume, surface, and radius of a droplet, σ_{SB} is the Stefan-Boltzmann constant. But in paper [13] a few orders of magnitude faster freezing of droplets seems has been observed; the frozen droplets reflect from a receiver while the molten - stick to it. May be this is because temperature of molten gold in the droplets produced by nanobumping is close to the melting temperature. Our molecular dynamics simulations presented below show that liquid in a dome and a jet shown in Fig. 1 are significantly overcooled below the melting temperature. Distances L_{dr} between a receiver and a donor plate in [13] were $L_{dr} \sim 10$ microns much less than $L_{dr} = 2$ mm in [14]. In [13] the time of flight $t_{frez} \sim 1 \cdot [(L_{dr}/10\text{um})/(v_{droplt}/10\text{m/s})]$ μs (to pass distance $L_{dr} \approx 10$ microns) divides molten and solid nanodroplets. In [14] nanodroplets were hotter, evaporative cooling enhances temperature decrease, and according to authors of paper [14] nanodroplets are still liquid after flying time 2[mm]/100[m/s]=20 μs.

The cooling time $t_{cond} = [R_L/(1\text{um})]^2/\ [\chi/(1\text{cm}^2/\text{s})]$= 10 ns due to conduction along high conductance metallic film is much shorter than the radiative and evaporative cooling times. This is why such a cooling is responsible for retention of the form of transient nanobump. Conduction along a film transfers heat from a hot spot $r < r_{delam}$ to the outside area $r > r_{delam}$, see Fig. 1. Thus this area serves as an infinitely capacious thermal sink. This means that we can influence the cooling of a nanobump by decreasing area or volume of cold metal external relative to the hot spot $r < r_{delam}$. The outside area may be done as a disk. We have to balance mechanical and thermal abilities of the disk varying its radius $R_{dsk} > r_{delam}$. From the one side the disk has to absorb mechanical momentum from a flying dome and to transfer it into a substrate, and from the other side the disk has to limit a cooling rate of a dome. Choice of material for substrate

---

[1] The direction of an illumination (from the vacuum side as in Fig. 1 a or through the transparent substrate) doesn't influence the subsequent dynamics if the energy homogenization across thickness of a film takes place prior to the onset of significant motion of a film. This is the case of the thin films, thinner than depth of a heat affected zone $d_T \approx 140$ nm for Au of an ultrashort laser pulse [9].

(low conductive glass versus high conductive crystallin silicon or diamond) also influence cooling ability. Using a film made of metallic alloys, like in the experiment [11] where Au/Pd alloy was used, with a low conductive component or pure metals like Pt, Fe with decreased heat diffusion coefficient χ is the another way to regulate thermal rate.

2. Resources required for molecular dynamics simulation

Number of atoms which might be involved in MD simulation can be determined by two geometrical parameters: radius R_L and thickness d_f of the metal film – see Fig. 1. One of the largest ($2r_{delam} \approx 20$ μm) and very accurate nanobumps with rich fine substructures have been obtained in the Livermore's experiments [6]. Typical diameters $2r_{delam}$ are ~ 5 μm [11–13, 16, 17]. There are also examples with smaller scales $2r_{delam} \sim 1$ μm [3, 12, 15–17]. Technically available diameters $2R_L$, see Fig. 1 (a), of laser beams are limited from the smallest scales by the diffraction limit $2R_L \sim \lambda$. From the opposite side, the largest diameters are defined by pulse energy and usually are as large as tens and hundreds microns. The minimal submicron values of $2r_{delam}$ may be achieved using ultraviolet lasers or higher harmonics.

Typical thicknesses of the thin metal films varies from 20 to 100 nm. There are $\sim 10 \times 10^9$ atoms within a cylinder of $\pi\,[r_{delam}/(1\mu\text{m})]^2\,[d_f/(50\text{nm})]$ covering the delaminated region. We have to triple this number to include the minimally thick glass substrate able to exclude the influence of the back reflection from the rear-side of the supporting glass layer onto process of delamination from substrate. This process lasts during an acoustic time scale t_s. It is necessary to follow this huge system along very extended time interval of the order of 100 ns and more. Typical time step of molecular dynamics (MD) simulation is ~ 1 fs. Thus $\sim 10^8$ steps are required. Taking into account that about 1 second is required to perform a step with MD system of 200,000 atoms on a single processor core, MD simulation of several billions of atoms during 10^8 steps would require hundreds of years on a cluster with 1000 cores.

Table 1. The double scaling map covered by the MD-MC runs, see also Fig. 2. Number of atoms N_{atom} involved in MD-MC simulation is given in 10^6 units. The simulation box is a square $L_b \times L_b$ in the plane of a contact. The sizes L_b and initial thickness d_f of a film are given in [nm]. The last column presents temperature T_{margn} in [K] of a thermostat acting in the margin area between the square $L_b \times L_b$ and a circle where a film separates from substrate, see Figs. 5 and 6.

#	N_{atom}	L_b	d_f	$v_{0\sigma}$	$v_{0\chi}$	[K]
20	6.0	140	5.1	2.6	6.3	500
23	6.0	140	5.1	2.6	3.1	500
30	44	270	10	3.6	6	500
3	192	620	8.3	2.6	∞	500
21	6.0	140	5.1	5.2	12.5	500
22	6.0	140	5.1	10	25	500
24	6.0	140	5.1	5.2	6.3	500
25	6.0	140	5.1	5.2	6.3	500
26	2.1	140	1.8	6.2	12.5	500
27	2.1	140	1.8	4	8.1	500
28	6.0	140	5.1	10	12.5	500
29	6.0	140	5.1	10	12.5	300
29a	6.0	140	5.1	10	12.5	300*
31	44	270	10	3.8	6.3	500

This difficulty is usual for MD applications - the spatial-temporal size of application is much larger than available algorithmic/computer resources. We have to use physics of nanobump phenomenon in an attempt to overcome this difficulty. Two steps to decrease the computational demands were used. Separation of the delamination process from the process of slow inflation of a nanobump is the first step. The second step is based on the self-similarity of the problem relative to the capillary and cooling parameters. The second step is presented in next Section. The splitting of the delamination and inflation processes (the first step) is a consequence of very large (three or more decimal orders) difference between durations of the delamination stage and the inflation and capillary deceleration stage. This large difference arises from the difference in scales and velocities. The size $R_L \sim 1 - 5$

μm is $F_x = 10 - 100$ times larger than film thickness $d_f = 20 - 100$ nm. The delamination is connected with rarefaction and compression waves, their interactions, and reflections from a glass/metal contact and a vacuum boundary of a film. The waves propagates distance d_f with elastic longitudinal sonic speed $c_s\sqrt{(K + 4G/3)/\rho} \approx 3.3$ km/s (for Au); here K, G are bulk and shear modulus. The speed c_s is $F_v = 30 - 100$ times higher than velocities 20-100 m/s of a film after its separation from a substrate. The large cumulative factor $F = F_x \times F_v$ means that we can with high accuracy split the delamination and the inflation of a nanobump, see [10]. We neglect curvature of film during delamination (this is one side) and the interaction of the delaminated film with substrate is absent after delamination (this the other side). Thus the inflation flight is simulated by MD without substrate. The substrate in a MD run serves only as a sink of momentum in the region near the point r_{delam} of attachment of a film to a substrate, i.e. near the lateral margins, see Fig. 1.

The delamination process is simulated with two-temperature one-dimensional hydrodynamics code [10]. This code is accurate, it includes full two-temperature physics, and it is inexpensive in the sense of the computer resources. The code is a very valuable addition to the MD code. Indeed, it is difficult to describe full two-temperature physics together with an electron pressure effects inside the MD subroutines. The hydrodynamics code supplies the MD simulation with the initial (for the MD code) temperature and velocity distributions along a film. This is the velocity distribution after delamination from substrate.

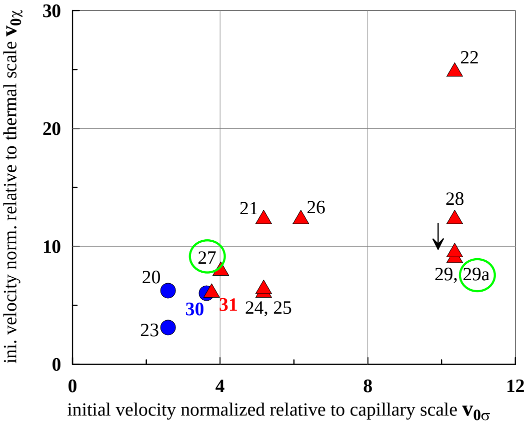

Figure 2. Performed MD-MC runs in plane of parameters. We vary ratio v_σ/v_χ in the range ~ 1 and vary ratio of initial velocity $v_c(0)$ to these velocities in a wider range. The blue circles corresponds to the first three lines in Table 1 presenting the non-ejecting (all matter of a film remains on substrate) cases. The numbers 27 and 29a with the circles around correspond to the cases shown in Figs. 3, 5 (#27) and 4, 6 (#29a).

3. Self-similarity thanks to capillary-cooling relation

3.1. Capillary dynamics.

Dynamics of molten film inside its circle $r < r_{delam}$ of separation from a substrate is determined by inertia and surface tension. The swelling film is clamped to the immovable circular arc with a radius $r = r_{delam}$ placed on an immovable substrate. Therefore a capillary force acting onto the attachment point $r = r_{delam}$ doesn't produce a work. As a result a sum of potential energy of surface tension $2\sigma S$ and kinetic energy

$$E_{kin} = (1/2)\int_0^{r.delam} \rho(r,t)d(r,t)\vec{v}^2(r,t)2\pi r dr$$

is conserved in time, here σ is a coefficient of surface tension, S is a surface area of a film inside the circle $r < r_{delam}$, the area is taken twice (coefficient "2") because there are two sides of a film; the integral is written for the 3D case with a circular illumination spot in Fig. 1, similar expression exists in the 2D case, r is a distance from a beam axis in Fig. 1, $\rho(r,t)$ is density of liquid gold. We neglect temperature and therefore density differences across thickness of a thin film: $\rho(\vec{r},t) = \rho(r,t)$. Value $d(r,t)$ is thickness of a film along a normal to the substrate surface. Surface tension acts as a spring decelerating and returning back a moving point mass attached to the end of a spring.

The film, clamped to the circular arc with a radius $r = r_{delam}$, oscillates in time above and below the plane of a contact if we imagine that the substrate disappears inside the circle

$r < r_{delam}$. In case of small initial velocities $v \ll v_\sigma$ a period of oscillation is $3.7 r_{delam}/v_\sigma$ [10]. The capillary velocity scale

$$v_\sigma = 2\sqrt{\sigma/(\rho d_f)} = 46\,[\sigma/(1000\mathrm{dyne/cm})]^{1/2}\,[\rho/(19.3\mathrm{g/cm^3})]^{-1/2}\,[d_f/(100\mathrm{nm})]^{-1/2}\ \ [\mathrm{m/s}] \quad (1)$$

is defined from expression $2\sigma = (1/2)\rho d_f v_\sigma^2$. Let's approximate the shape of a nanobump by a cone and a velocity distribution by a monotonous function $|\vec{v}| = v_c[\cos(\pi r/(2r_{delam}))]^2$ having the maximum value v_c in the tip and going to zero in the attachment point r_{delam}. Using an expression for a lateral area of a cone and integrating kinetic energy, we rewrite an energy conservation in a form

$$2\pi r_{delam}\left(\sqrt{h_c^2(t) + r_{delam}^2} - r_{delam}\right)\sigma + (1/2)\,2\pi\,(3/16 - 1/\pi^2)\,\rho_0\,d_f\,r_{delam}^2\,[v_c^2(t) - v_c^2(0)] = 0, \quad (2)$$

where $h_c(t), v_c(t)$ are the height of the tip above the initial contact plane and velocity of the tip. Energy equation (2) relates the current height h_c and velocity v_c : velocity decreases as the height and hence surface area and surface energy increase. The maximum height h_{max}, achieved in a stopping point $v_c(t_{stop}) = 0$, is

$$h_{max}/r_{delam} = v_{0\sigma}\sqrt{\alpha\,(2 + \alpha\, v_{0\sigma}^2)}, \quad \alpha = 0.172, \quad v_{0\sigma} = v_c(0)/v_\sigma. \quad (3)$$

In (3) the non-dimensional initial velocity $v_{0\sigma}$ is normalized relative to the capillary scale (1), α is a numerical coefficient. For the moderate values of velocity $v_{0\sigma} \leq 1$, the turning instant

$$t_{stop} = 20\,[r_{delam}/(1\,\mu\mathrm{m})]\,\sqrt{[d_f/(100\,\mathrm{nm})][\rho/(19.3\,\mathrm{g/cm^3})]/[\sigma/(1000\,\mathrm{dyne/cm})]}\quad [\mathrm{ns}]$$

weakly depends on velocity $v_{0\sigma}$ and is approximately a quarter of a period $3.7 r_{delam}/v_\sigma$.

We see that it should be $v_{0\sigma} \sim 1$ to lift up the tip of a nanobump to the height $h_{max} \sim r_{delam}$. To take the integral of kinetic energy, we suppose that (i) $\rho(r,t) \approx \rho_0$ (19.3 g/cm^3 for Au), that (ii) $d_f(r,t) \approx d_f$, and (iii) we neglect dispersion of velocities in the vicinity $\sim d_f$ of the point $\vec{r}$ of the film, here d_f is initial thickness of a film. The assumption about density is approximately valid because our simulations show that in the nanobumping regimes the temperatures of a film shortly (at a $\sim$ 100 ps time scale) after irradiation are below 2 kK and thermal expansion is relatively low: density at the boiling curve is $\rho_2 = \rho_{bin}(T = 2\mathrm{kK}) \approx 16.8$ g/cm^3 according to a wide-range equation of state for Au [18, 19], see also [20], thus $(\rho_0 - \rho_2)/(\rho_0 + \rho_2) = 0.07$. Energy conservation $2\sigma S + E_{kin}$ =const is valid but the assumption (ii) $d_f(r,t) \approx d_f$ is only approximately accurate as long as the stretching of a film is small. The stretching is small if velocity is small $v_{0\sigma} \ll 1$. There is significant stretching for the larger velocities $v_{0\sigma} \sim 1$ and higher (nonlinear regimes).

It is important that the stretching becomes very inhomogeneous in the nonlinear regimes. This is a consequence of a strong mass redistribution along a film. Central part of a film forms a droplet (in 2D [10, 20]) or a jet [or a jet plus droplet(s) in 3D] thus doing stretching very inhomogeneous - there are condensations (droplet or jet), from the one side, and strong stretching and thinning of the film remaining outside relative to the condensations, from the other side. Extremely long jet (many lengths r_{delam}) may be developed. The rate per unit of mass of transfer of kinetic energy into the surface energy decreases in a jet because surface to volume ratio decreases from film to jet. Nevertheless, surface tension will return fluid back for arbitrary large initial velocity $v_{0\sigma}$, because surface area grows with stretching while kinetic energy causing stretching is limited. Of course, this is true in the case of infinite stretchability of a film and a jet - there is no breaking of surface of a film or decay of a jet into droplets. In reality the jet formation process, stretching and thinning of a film, and rupture of a film or a jet together with interplay with a recrystallization wave make up a set of rather complicated regimes considered below in Chapter 5.

3.2. Cooling rate. Hot spot created by an ultrashort laser impact onto a metal film cools down as a result of conductive heat transfer along a film from the hot spot to the external area of a film, see Section 1. The temperature decrease causes crystallization of a film and a jet. Transition to a solid state sharply changes mechanical properties - polycrystalline solid strongly resists to stretching, while liquid resists weakly, only through surface tension. This jump of stretchability is a reason of dynamic phenomena near the solid-liquid crystallization zone, e.g., breaking of a liquid film surrounding growing crystal grains, or rupture of a very much thinned solid film under action of significant inertial forces stretching solid, see Sections 5 and 6 below.

Cooling in a 3D case is described by a heat conduction equation $T_t = (\chi/r)(r\,T_r)_r$, here $T_t \equiv \partial T/\partial t$, $T_r \equiv \partial T/\partial r$, r is a cylindrical radius, $\chi = \kappa/c$ is a heat diffusion coefficient, κ, c are heat conduction coefficient and heat capacity per unit of volume. Transmission of heat along distances $\sim R_L$ becomes significant much later after finishing of a two-temperature stage, therefore usual well-known values of the coefficients χ, κ, c have to be used. For simplicity the moderate dependencies of these coefficients on temperature are not included for our temperature range in the expressions below. A heat equation has a fundamental solution (thermal Green function)

$$T(r,\tau) = \frac{E}{\pi\, c\, d_f\,(4\,\chi\,\tau)} \exp\left(-\frac{r^2}{4\,\chi\,\tau}\right), \tag{4}$$

describing diffusion of heat along a film after impulsive absorption of energy E [erg] in the point $r = 0$ in the instant $\tau = 0$.

Ultrashort pulse laser illumination shown in Fig. 1 (a) creates similar to (4) Gaussian one-temperature $T_e = T_i$ distribution in a short time scale 5-7 ps. Short duration of this stage prevents lateral expansion of heat during the first few tens of picoseconds. The Gaussian temperature profile made by laser is

$$T(r, t=0) = \frac{E}{\pi\, c\, d_f\, R_L^2} \exp\left(-\frac{r^2}{R_L^2}\right). \tag{5}$$

Diffusive spreading of the profile (5) outside on the distances $\sim R_L$ takes tens of nanoseconds for $R_L \sim 1$ micron and usual values of thermal diffusivity $\chi \sim 1$ cm^2/s. In this regard it is written $t = 0$ in expression (5): ps is much shorter than ns. Around the instant $t = 0$ laser action takes place. There is a time lag between the instants $\tau = 0$ and $t = 0$. There is the *same* absorbed energy E in expressions (4) and (5).

Comparing expressions for the Green function (4) and for the initial deposition (5) we write solution of a Cauchy problem for heat conduction equation with initial data given by expression (5). The solution

$$T(r,t) = \frac{E}{\pi\, c\, d_f\,(R_L^2 + 4\,\chi\, t)} \exp\left(-\frac{r^2}{R_L^2 + 4\,\chi\, t}\right), \quad T(r=0,t) = \frac{E}{\pi\, c\, d_f\,(R_L^2 + 4\,\chi\, t)} = \frac{T_c}{1 + 4\chi\, t/R_L^2} \tag{6}$$

describes evolution of a temperature field after laser action $t > 0$. Dependance presenting decrease of temperature in the tip point $T(0,t)$ is also given in (6).

There are the delamination r_{delam} and the melting r_m circles corresponding to the delamination F_{delam} and melting F_m thresholds on an absorbed fluence distribution $F = F_c \exp(-r^2/R_L^2)$; namely this absorption produces the initial temperature field (5); $F_c = E/(\pi\, R_L^2)$. The delamination F_{delam} threshold is below the melting threshold F_m in the case of weak adhesion between gold and a glass substrate, i.e., $r_m < r_{delam}$. We are studying formation of a nanobump with some substructure in the tip, see Fig. 1 (c-h). This is possible if a film in a hot spot transits to a liquid stage. Thus we are interested in the cases $F_c > F_m$.

A solid film weakly departs from a substrate surface. Thus the radius r_m should be regarded as a "true" or significant delamination radius. It marks position where an enhanced separation of a film from a substrate begins. A nanobump inflates mainly inside a circle $0 < r < r_m$. This means that these nanobumps after laser action have

$$T(r=0,t=0) \equiv T_c(t=0) = E/(c\,d_f\,\pi\,R_L^2) = F_c/(c\,d_f) > T_m,$$

i.e., their tip temperatures are above the melting threshold, see (6). Let's estimate duration t_{sol} necessary for total solidification: $T_c(t_{sol}) = T_m$, where T_m is melting temperature. From equation (6) we obtain

$$t_{sol} = [(T_c(t=0) - T_m)/T_m]\,R_L^2/(4\chi). \tag{7}$$

Expression (7) shows how the solidification time increases above a melting threshold. Estimates and simulations show that a degree above the melting threshold $T_c(0)/T_m$, where nanobumps shown in Fig. 1 (c-g) exist, is limited by a value $T_c(0)/T_m \approx 2-3$. Above this limiting value a hole shown in Fig. 1 (h) appears. Initial local temperature T of a film depends on local absorbed fluence $T = F/(d_f\,c)$. The initial (later in time whole nanobump will cool down and freezes) radius r_m is defined by the degree $T_c(0)/T_m$:

$$T_m(r_m,t=0) = T_c(0)\exp(-r_m^2/R_L^2), \qquad r_m = R_L\sqrt{\ln(T_c/T_m)}.$$

Let's define cooling velocity v_χ and initial velocity normalized relative to v_χ as this is done in expressions (1) and (3). We have

$$v_\chi = \chi/R_L = 100\,[\chi/(1\,\mathrm{cm}^2/\mathrm{s})]\,/\,[R_L/(1\,\mu\mathrm{m})]\ \ [\mathrm{m/s}], \qquad v_{0\chi} = v_c(t=0)/v_\chi. \tag{8}$$

3.3. Double scaling and reduction of demands on computer resources.

Now we have two non-dimensional parameters $v_{0\sigma}$ (3) and $v_{0\chi}$ (8). In next Section the Monte-Carlo method used in the molecular dynamics algorithm MPD^3 [21] is presented. It allows to include an electron heat conduction into simulations. It is possible to vary a heat conduction coefficient κ in the Monte-Carlo method. This freedom together with the two non-dimensional parameters (3) and (8) give us ability to simulate a huge experimental object with a smaller molecular dynamics (MD) object, see Chapter 2.

Let's illustrate this with an example. The experimental object is: $R_L = 1$ micron, $v_c(t=0) = 100$ m/s, $\chi = 1$ cm^2/s, $\sigma = 1000$ dyne/cm, $d_f = 60$ nm, $T_c(t=0) = 2000$ K. Then the parameters (3) and (8) are: $v_{0\sigma} = 1.68$, $v_{0\chi} = 1$.

Let's choose the simulation object having the same temperature distribution and values of $v_{0\sigma}$ and $v_{0\chi}$ but ten times smaller geometrical values R_L and d_f; thus it is three order of magnitudes smaller in number of atoms. To do this we have to adjust initial velocity $v_c(0)$ and χ; heat capacity is the same in experiment and in MD, therefore changing κ is equivalent to the changing of χ. We have to take into account that in the used EAM (embedded atom method) interatomic potential of Au [22] the coefficient σ is 540 dyne/cm [10].

Calculating, we find parameters for our equivalent MD object: $v_c(0)|_{MD} = 229$ m/s and $\chi|_{MD} = 0.1$ cm^2/s.

4. Numerical simulation of conductive cooling

Approach used here combines multi-processor molecular dynamics (MD) algorithm MPD^3 [21] and Monte-Carlo method necessary to describe heat conduction. In the general case of a laser-matter interaction the energy of a laser pump is absorbed by electrons in a skin layer, and then

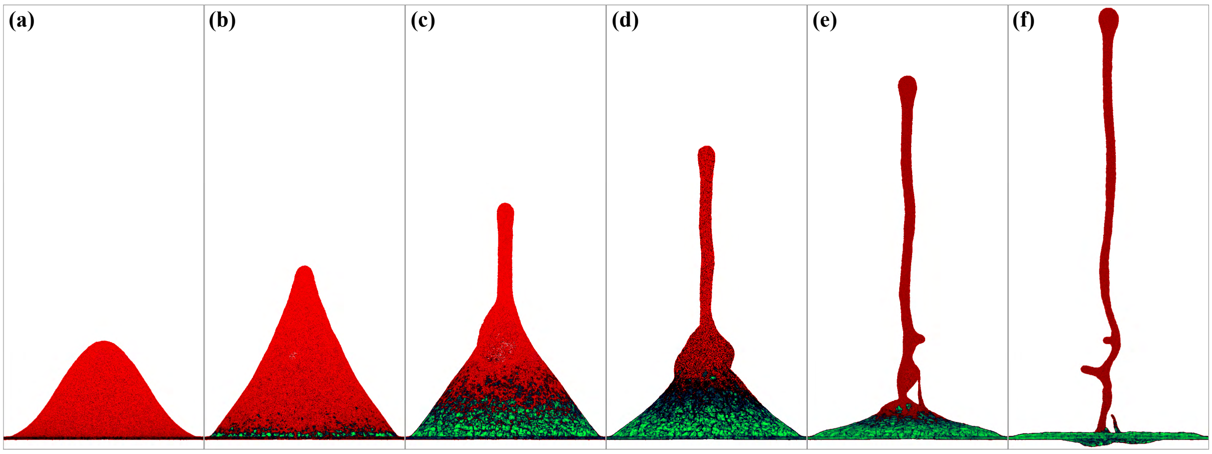

Figure 3. Evolution of nanobump in the case #27, see Table 1. Capillary forces decelerate inflation of the nanobump shell. Therefore the tip of nanobump (not the tip of jet) stops rising and turns back. It impacts the surface of substrate, compare with experimental pictures [6, 7]. This is obvious because the shell is seen below the plane of substrate in the last frame. In simulation we do not put a barrier in the plane of initial gold-glass contact. Thus the material can move through this plane in simulation. Contraction of surface area of solidified shell (the height of the cone decreases) will inevitably lead to formation of the radial folds seen in experiments, e.g., [6, 7]. The folds accept the excess of solid surface area of the thin shell. The shape of nanobump changes during its motion from convex to conical one. This is a result of pumping of mass into jet. Thus the region of attachment of the shell to the bottom of the jet is the main region resisting to the back motion of the shell because inertia of a massive jet is large relative to inertia of a strongly thinned shell - a jet strains a shell giving a conical shape to the shell. The lateral subjet like protrusions results from breaking of a moving, stressed, and solidifying liquid-solid shell (green is solid, red is liquid). Evolution of the protrusions covers the frames (c-f), see also Fig. 5 below. Shown frames correspond to the times: (a) $t = 72$ ps, (b) 144 ps, (c) 216 ps, (d) 290 ps, (e) 380 ps, (f) 475 ps.

the electron-ion coupling and electron heat transport are described by Monte-Carlo method (MC). In this paper MD-MC code is employed to follow one-temperature dynamics and cooling of the nanobump long after the short stages of absorption of laser energy and two-temperature relaxation.

To combine MC with MD the light Monte-Carlo particles, treated as classical “electrons”, were added to atom subsystem. Each host atom/ion has one “electron”, which has its own velocity but its position is always allocated on its host atom. It guarantees the charge neutrality in the combined electron-ion system in any conditions. The neighboring atoms exchange their electrons with some frequency determined from known experimentally thermal conductivity of liquid gold at the melting point. The pair of atoms, where electron-electron exchange takes place, is chosen randomly from the Verlet list of neighbors within a cutoff distance.

In addition to the frequency of electron-electron exchange between atoms, we adjusted the mass of “electron”, in order to obtain the characteristic time of electron-ion energy exchange in e-i collisions. The electron-ion scattering depends on the velocity vectors of electron with mass m_e and ion with mass m_i according to equations:

$$\begin{aligned} \mathbf{v}'_e &= (m_e\mathbf{v}_e + m_i\mathbf{v}_i + m_i v\mathbf{n})/(m_e+m_i) \\ \mathbf{v}'_i &= (m_e\mathbf{v}_e + m_i\mathbf{v}_i - m_e v\mathbf{n})/(m_e+m_i) \end{aligned} \quad (9)$$

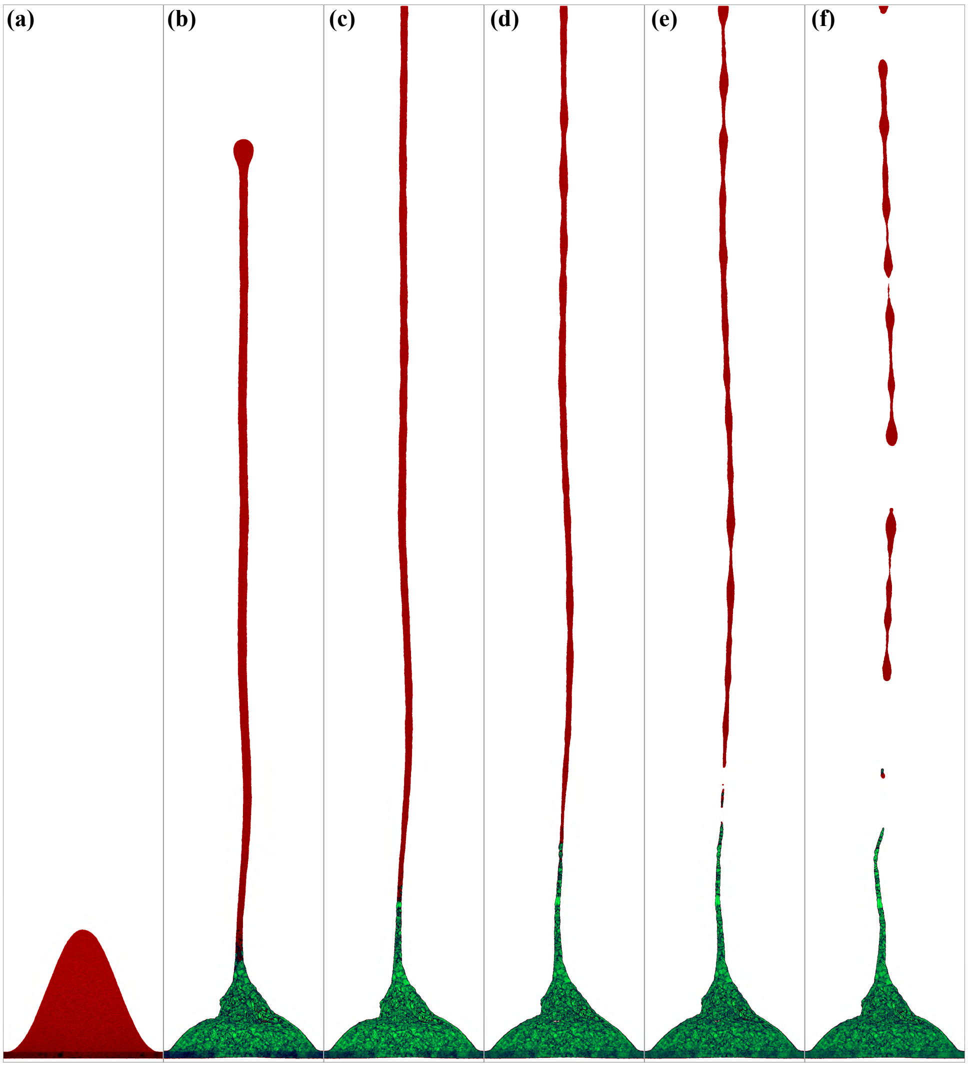

Figure 4. The case #29a, see Table 1. (a) $t = 72$ ps, (b) 650 ps, (c) 860 ps, (d) 1.1 ns, (e) 1.3 ns, (f) 1.5 ns.

where v is an electron-ion relative speed, and $\mathbf{v}'_e$ and $\mathbf{v}'_i$ are the velocities of electron and ion in the laboratory system after collision. The unknown unit vector $\mathbf{n}$ is assumed to be distributed isotropically and can be provided by a generator of random directions. Equations (9) conserve the total momentum and energy of electron and ion subsystems.

The described Monte-Carlo method has free parameters of effective electron mass m_{ef}, electron jump rate ν_D, and e-i-collision rate ν_{ei}. For simplicity the jump and e-i-collision rates are assumed to be equal $\nu = \nu_D = \nu_{ei}$ in this Monte-Carlo model. Thus, both electron diffusion and e-i energy exchange depend on the jump/collision rate ν. Furthermore, the e-i energy exchange rate depends on effective electron mass. Because electron thermal conductivity λ_e is only guided by ν and independent on m_{ef} in equilibrium systems where local condition $T_e = T_i$ is hold everywhere, the time-independent solution of heat equation is used first to fit ν with the known experimental thermal conductivity.

To find ν the steady MC-MD solutions of the Fourier law for the heat flux $q = -\lambda\, dT/dx$ is tested in a domain bounded by two subdomains, where the different temperatures 1300K and 1200K are supported by two electron thermostats separated by a layer of 100 nm thick.

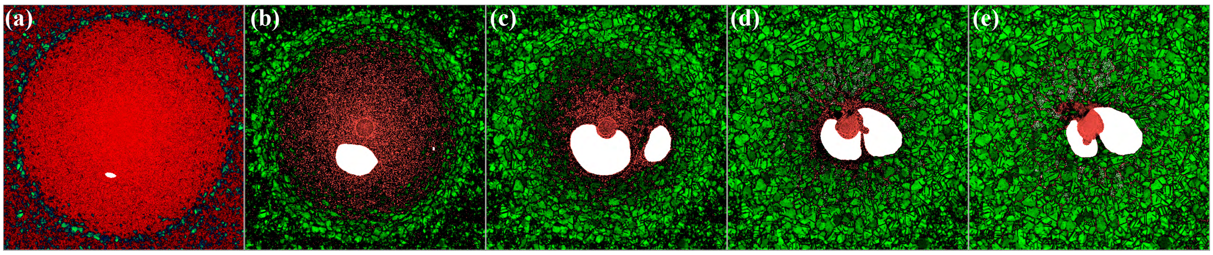

Figure 5. The run # 27. This is a top view from the upper point onto the plane of a film, see also the side view for the same run in Fig. 3. The instants (a) $t = 144$ ps, (b) 200 ps, (c) 270 ps, (d) 380 ps, and (e) 475 ps are shown. A map of the symmetry parameter is given: solid is green, liquid is red. We see definite difference between the margins and the central circle where a film delaminates from a substrate. The thermostat is working in the marginal area covering space from the sides of the square to the circle arc path. The thermostat absorbs momentum coming through the surface tension force and absorbs heat flux flowing from the hotter central part. The film was initially very thin in the runs 26 and 27, see Table 1. Of course, in a thinner film the decay processes proceed more easy. Thus the MD-MC simulation reveals appearance/disappearance of the atomic size holes in a very thin film as a result of thermal fluctuations. One of them crosses a metastable barrier and transforms into the viable expanding nucleus, see frame (a). Later another one appears, see frame (b). It is interesting, that appearance of the holes doesn't mean automatically termination of the inflation/deceleration development of a nanobump or immediate total rupture. A hole expands with moderate velocity, this conclusion follows from the calculations performed in [10].

After attainment of steady linear temperature profile with constant temperature gradient $dT/dx = 1 \times 10^9\,[\mathrm{K/m}]$ within the layer, the time-averaged heat flux was calculated during 300 ps of MD-MC simulation. To provide the experimental flux the electron jump rate $\nu = 4.286 \times 10^{15}\,[1/\mathrm{s}]$ was found to have been used in MC part of our combined MC-MD simulation of gold.

After determining the jump rate, the effective mass of "electron" was fitted to the relaxation time between electrons and ions obtained from the 2T model equations for evolution of electron T_e and ion T_i temperatures. In the case of a sample with uniform density and temperature where material is staying at rest, the 2T hydrodynamics model equations transform to the system of two coupled kinetic equations for temperatures $T_e(t)$ and $T_i(t)$ given by

$$c_e dT_e/dt = -\alpha\,(T_e - T_i), \qquad c_i dT_i/dt = +\alpha\,(T_e - T_i),$$

where c_e and c_i are electron and ion heat capacities, respectively, and α is an electron-ion coupling coefficient. Solutions of above equations gives the relaxation time of 5 ps. The same time can be achieved in MC-MD simulation if $m_{ef} = 6m_e$ of standard electron mass is used.

To simulate atomic motion in gold under high strain-rate deformations we use the well-fitted EAM potential [22], which was successfully utilized in [3, 9]. This EAM potential reproduces mechanical response of gold to strong compression and stretching, and the melting point as well.

5. Dynamics of inflation, deceleration and decay of nanobump in liquid or solid states

Using a series of two-temperature 1D hydrodynamics and MD-MC runs we have investigated the parameter space of a nanobump problem relative to the capillary $v_{0\sigma}$ (3) and thermal $v_{0\chi}$ (8) numbers. A set of the MD-MC runs is listed in Table 1 and in Fig. 2. The small initial

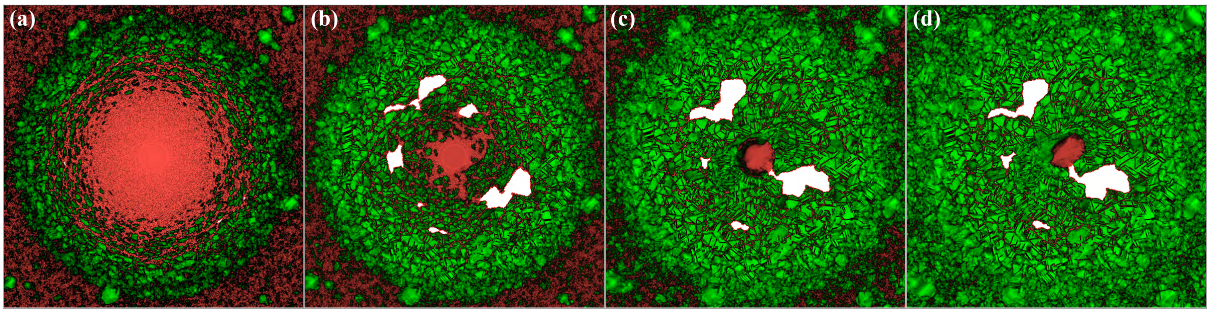

Figure 6. The top view onto dynamical and thermal processes going in the moving shell in the run #29a. Fluid is strongly overcooled and the two free surfaces are near to the overcooled volume (crystallization of a thin film) therefore crystallites nucleates inside molten gold. At the early stage (frame a), when area of a liquid shell constitutes the significant portion of a bump, there is a wide transition belt around the liquid portion of the shell. The crystal grains in the belt seems elongated in the azimuthal direction - this is a result of projection of the inclined lateral side of a dome onto plane of view. (a) $t = 230$ ps, (b) 360 ps, (c) 720 ps, (d) 1.8 ns.

velocity $v_c(t = 0)$ cases are located near the origin point in Fig. 2. They have been discussed in Subsections 3.1 and 3.2 above. In those cases a rupture from substrate and strong mass redistribution along a film are absent. At larger velocities $v_c(0)$ a nanobumps with a nipple type apex shown in Fig. 1 (c) are formed (the cases 23, 30 in Fig. 2). A rather short jet with a frozen droplet at the upper point of the jet is formed in the case 20. Length of this rather short jet is slightly above the radius of a nanobump at the contact plane. The group of the relatively low velocity runs is highlighted in Fig. 2 by blue color (the blue circles). The group 20, 23, 30 is separated from the other runs because in the cases 20, 23, 30 the whole of metal remains on the substrate.

The runs selected by the red triangles in Fig. 2 corresponds to the cases when part of a mass of a film loses its contact with a film and flies away. Transition between these ejecting and non-ejecting regimes is abrupt. This follows from a comparison of the runs 30 and 31. Small 5% increase of initial velocity $v_c(0)$ provokes sharp changes from a compact nanobump 30 with a moderate mass redistribution and a nipple apex to the case 31 with a strongly thinned shell of a nanobump and a massive very long jet.

To start the MD-MC runs an initial state has been prepared. The preparation involves heating and melting of a gold film by a Langevin thermostat. The thermostat creates a distribution of temperatures with a maximum temperature 2000 K in the central point. Temperatures decrease from 2000 K in the center to 1500 K in the margin. After that a hydrodynamic velocity distribution having only a normal component relative to the surface is imposed. The maximum velocity is velocity of a tip $v_c(0)$. Velocities decrease down to zero in the margin. After beginning of a run, the thermostat is removed everywhere except the margin. In the margin the thermostat holds a film at the margin and supports the margin temperature T_{margn} at a given level below a melting point. This temperature is given in the last column of a Table 1. It was $T_{margn} = 500$ K for all runs listed in Table 1 except the runs #29 and #29a; $T_{margn} = 300$ K for these runs. Temperature difference between the central part of a nanobump and the margin supports the cooling flow and cools down the central part, see Subsection 3.2. Gradually a recrystallization zone moves up from the margin to the central part - solidification of a nanobump proceeds, see Figs. 3-6 where the green color corresponds to solid, while the red color highlights molten gold.

Decreasing of the margin temperature T_{margn} intensifies the cooling flux, thus increasing rate of solidification. This essentially increases the thermal velocity scale v_χ (8) and decreases normalized velocity $v_{0\chi}$ (8). Estimates based on a thermal equation discussed in Subsection 3.2 give 25% reduction of the parameter $v_{0\chi}$ as a result of changing $T_{margn} = 500$ K → 300 K. This reduction is marked by the arrow in Fig. 2. In all other respects the runs 28, 29 and 29a are identical, see Table 1.

Another fine difference was tested in the runs 29 and 29a. Working of a thermostat in the margin area prevents freezing of fluid in this area because a stronger thermostat faster destroys atom-atom correlations directed to nucleation of lattice seeds thus impeding the crystallization, see Figs. 5 and 6. To check an influence on results, we increase 1.5 times the characteristic time of thermostat from 0.8 ps for all runs to 1.2 ps in the particular run 29a. An influence on dynamics of a nanobump is small.

Figs. 3 (#27) and 4 (#29a) show the side view of the process. These runs are in ejecting regime. In this regime large amount of mass is pumped from the nanobump shell into the jet. As a result there is strong thinning of a shell and very long jets develop. The thinning proceeds while a shell is in a liquid state or, when solidification begins, the thinning takes place in the liquid part of a film. The runs 27 and 29a have approximately similar cooling rates but the capillarity effects are weaker in the case 29a, comp. the marked points 27 and 29a in Fig. 2. This follows from the difference in the value $v_{0\sigma}$ (3). Therefore the jet 29a is longer. It begins to break into separate subjets and later decays into droplets as a consequence of elongation and Rayleigh instability.

Excess of kinetic energy above a binding initial surface energy defines a measure of kinetic deformations of a bump - larger excess - then longer jets, and then the decay processes become more active, see Subsection 3.1 about conservation of energy and Fig. 1. Comparing Figs. 3 and 4, we see how this excess works. The jet in Fig. 4 becomes thinner in its bottom part as a result of weakening and termination of supply from the shell when the crystallization process gradually covers whole shell. This decreasing feed together with elongation of a stretching jet and tearing off the subjet form the narrow peaked frozen jet in the apex of a bump. Separated hot droplets slowly cool down, see Chapter 1. Frozen shell is made from a dense set of the very small size nanocrystallites, comp. with [3]; colorizing presents distribution of a symmetry parameter: green is solid, red is liquid. The set is formed in the process of crystallization of strongly overcooled liquid gold. Thin overcooled liquid shell has two free surfaces, therefore the solid grains begin to grow in liquid at some distance from the continuous solid film, see Fig. 6 below. The green shell in Fig. 4 has holes, see also Fig. 6 below. Such holes are often observed in experiments, see, e.g., [7].

Why experimentally the frozen bumps are observed only in the cases with tight focusing when a radius of a nanobump $\sim R_L$ is small? This is a result of interplay between the value of a heat conduction coefficient κ and the size R_L limited from the small sizes by an optical wavelength ~ 1 micron. Relative thickness d_f/R_L is also significant. Because for the large spots when R_L is tens and hundreds microns the relative thickness is small. Relative thickness d_f/R_L usually cannot be larger than d_T/R_L, where d_T is thickness of a heat affected zone. This limit will meet us if we attempt to increase film thickness and overcome the value d_T. Typical values are $d_T = 30 - 130$ nm for different metals. It should be emphasized that in the case $d_f > d_T$ the bump shell may spall out not at a contact but inside a film [8]. The shell made from the spallation plate has significant thickness inhomogeneities because this is the case of nucleation inside a film relative to the case of a spall from a very smooth contact with substrate. Of course, the inhomogeneities accelerate decay of the bump shell into cloud of the spatially separated droplets [14]. Flight of a hollow liquid bump or a dome or a cupola [23] created from the *bulk* targets is observed beginning from the first paper [24] thanks to microinterferometric pump-probe technique.

Duration of flight usually is 1-10 ns, and flight distance is $\sim 10\%$ of $R_L \sim 100$ microns in these experiments. Initial velocity usually is rather large $v_c(0) \sim 0.1 - 1$ km/s, while the capillary scale (3) $v_\sigma \sim 10-100$ m/s is smaller if the shell is thicker. Thus it is difficult to observe the capillary deceleration of larger cupola: inflation velocity $v_c(t)$ should decrease per one unit of v_σ for every one unit of a large flight distance $\sim R_L$. Therefore the jet formation and transformation of shell shape from a convex parabolic cupola to a cone (see Fig. 3) do not have time to realize before the shell rupture.

The conduction coefficients κ and χ of metals are fixed (usually $\kappa = 30-300$ W/m/K for solid metals). Therefore the thermal velocity scale $v_\chi = \chi/R_L$ (8) strongly decreases for large spots. Corresponding points have similar values $v_{0\sigma}$ as shown in Fig. 2, but the values $v_{0\chi}$ are much higher. In these conditions only a frozen ring around a delamination circle remains. This ring is observed in all experiments with the large spots. The ring presents the solidified remnants of marginal part of the entire shell. The central part of shell is torn off from the margin part and flies away. This situation is similar to the case of so called ”nano-crown” shown in Fig. 1 (h) but now at much larger scale R_L.

6. Non-equilibrium crystallization of thin film in conditions of strong and fast continuous stretching

Cooling and propagation of the recrystallization zone over a shell surface are shown in Figs. 5 (#27) and 6 (#29a). They correspond to the side view of the dynamic and thermal evolution presented in Figs. 3 (#27) and 4 (#29a). This is a non-equilibrium phase transition with a wide transformation belt separating pure liquid and pure solid. The belt is filled with a two-phase solid-liquid mixture. The newborn crystallites seems elongated perpendicularly to the radial direction because the lateral side of a shell is oblique relative to the plane of projection in Figs. 5 and 6.

The runs #27 $d_f = 1.8$ nm and #29a $d_f = 5.1$ nm have different thickness. It is easier to break a hole through a film in the case of a thinner film. In the run #27 shown in Figs. 3 and 5 the holes appear in the pure liquid. While in the run #29a (Figs. 4, 6) there are a liquid films surrounding the crystal grains. Stretching of a belt of a two-phase solid-liquid mixture stretches the liquid film in between the grains remaining the grains much less stretched. Therefore decrease of thickness of liquid is enhanced in the intergrain space. This process leads to formation of the holes penetrating through the pieces of the liquid film in the intergrain area, see Fig. 6 (b). The holes gradually grow and crystallize inside the solid bump.

7. Conclusion

We used Lagrangian hydrodynamics and molecular dynamics combined with Monte-Carlo codes to shed light onto the 3D processes initiated by an ultrafast laser action on the films deposited on substrates. New results (relative to [10]) about physics of formation of the bumps, including description of the thermal part of the problem discussed in Subsection 3.2., were obtained. Thermal problem should be solved in conjunction with the inertia/capillarity dynamical part of the problem. We use two non-dimensional parameters and scaling (see Section 3, Table 1, and Fig. 2), bypassing difficulties connected with the huge size for MD simulation of the considered experimental situation, see Section 2.

Acknowledgments

Authors acknowledge support from Russian Science Foundation (RSCF) (project No. 14-19-01599).

References

[1] F. Korte, J. Koch, and B. N. Chichkov, Appl. Phys. A **79**, p. 879 (2004)
[2] Y. Nakata, T. Okada, and M. Maeda, Jpn. J. Appl. Phys. **42**, L1452 (2003)

[3] D. Ivanov, A. Kuznetsov, V. Lipp, B. Rethfeld, B. Chichkov, M. Garcia, and W. Schulz, Appl. Phys. A. **111**, p. 675–687 (2013)
[4] A. Kuchmizhak, A. Ionin, S. Kudryashov, S. Makarov, A. Rudenko, Y. Kulchin, O. Vitrik, and T. Efimov, Optics Letters **40**, p. 1687–1690 (2015)
[5] M. Domke, S. Rapp, and H. Huber, Physics Procedia **39**, p. 717–725 (2012)
[6] M. Armstrong, *The evolution of ultrafast compression,* SIMES Seminar, (2015) https://simes.stanford.edu/events/mike-armstrong-simes-seminar
[7] D. Wortmann, J. Koch, M. Reininghaus, C. Unger, C. Hulverscheidt, D. Ivanov, and B.N. Chichkov J. Laser Appl. **24,** 042017 (2012)
[8] N.A. Inogamov, V.V. Zhakhovsky, V.A. Khokhlov, K.V. Khishchenko, Y.V. Petrov, D.K. Il'nitsky, K.P. Migdal, www.chemphys.edu.ru/pdf/2014-11-29-005.pdf (in Russian)
[9] B.J. Demaske, V.V. Zhakhovsky, N.A. Inogamov, I.I. Oleynik, Phys. Rev. B **82,** 064113 (2010)
[10] N. A. Inogamov, V. V. Zhakhovskii, and V. A. Khokhlov, JETP **120**, p. 15–48 (2015)
[11] V.I. Emelyanov, D.A. Zayarniy, A.A. Ionin, I.V. Kiseleva, S.I. Kudryashov, S.V. Makarov, T.H.T. Nguyen, A.A. Rudenko, JETP Lett. **99,** No. 9, p. 518–522 (2014)
[12] A.I. Kuznetsov, J. Koch, B.N. Chichkov, Appl. Phys. A **94,** p. 221–230 (2009)
[13] A.I. Kuznetsov, J. Koch, B.N. Chichkov, Optics Express **17,** No. 21, p. 18820–18825 (2009)
[14] C.M. Rouleau, C.-Y. Shih, C. Wu, L.V. Zhigilei, A.A. Puretzky, and D.B. Geohegan, Appl. Phys. Lett. **104,** 193106 (2014)
[15] P.A. Danilov, E.A. Drozdova, A.A. Ionin, S.I. Kudryashov, S.B. Odinokov, A.A. Rudenko, V.I. Yurovskikh, D.A. Zayarny, Appl. Phys. A **117,** 981–985 (2014)
[16] C. J. Koch,L. Overmeyer, and B. Chichkov, Optics Express **20**, p. 24864 (2012)
[17] A.I. Kuznetsov, C. Unger, J. Koch, B.N. Chichkov, Appl. Phys. A **106,** 479–487 (2012)
[18] A.V. Bushman, G.I. Kanel', A.L. Ni, and V.E. Fortov, *Intense Dynamic Loading of Condensed Matter* (Taylor & Francis, London, 1993).
[19] http://teos.ficp.ac.ru/rusbank/
[20] N.A. Inogamov and V.V. Zhakhovskii, JETP Lett. **100,** No. 1, p. 4–10 (2014)
[21] V. Zhakhovskii, K. Nishihara, Y. Fukuda, S. Shimojo, T. Akiyama, S. Miyanaga, H. Sone, H. Kobayashi, E. Ito, Y. Seo, M. Tamura, and Y. Ueshima, IEEE Proceeding of the 5th International Symposium on Cluster Computing and Grid (CCGrid 2005), May 9-12, 2005, (Cardiff, UK), Vol. 2, p. 848–854 (2005)
[22] V.V. Zhakhovskii, N.A. Inogamov, Yu.V. Petrov, S.I. Ashitkov, K. Nishihara, Appl. Surf. Sci. **255,** No. 24, p. 9592–9596 (2009)
[23] N.A. Inogamov, Yu.V. Petrov, S.I. Anisimov, A.M. Oparin, N.V. Shaposhnikov, D. von der inde, J. Meyer-ter-Vehn, JETP Lett. **69,** No. 4, p. 310–316 (1999)
[24] K. Sokolowski-Tinten, J. Bialkowski, A. Cavalleri, D. von der Linde, A.M. Oparin, J. Meyer-Ter-Vehn, S.I. Anisimov, Phys. Rev. Lett. **81,** 224–228 (1998)